nature communications

Article | Article in Press

https://doi.org/10.1038/s41467-026-77422-2

Harvesting environmental circadian oscillations for energy autonomy of soft robots

Received: 8 August 2025

Accepted: 20 August 2026

Published online: 07 September 2026

Check for updates

Sergio Picella[1,2], Alberto Comoretto[1], Olivier Vaarkamp[1,2] & Johannes T. B. Overvelde[1,2]

Energy autonomy remains elusive in soft robotic devices, yet is essential for real-world operation beyond laboratory environments. Existing onboard energy-source strategies for air-powered soft robots require manual intervention for long-term use. We propose a thermopneumatic strategy that exploits circadian thermal oscillations and a pneumatic control circuit to enable energy autonomy in soft robotic systems. Our thermodynamic cycle harvests environmental thermal energy, stores it as pneumatic pressure, and autonomously discharges it to power soft pneumatic devices. Using a low-boiling-point fluid, our design repeatedly generates sufficient energy for pneumatic soft robots. Our model indicates this strategy is applicable worldwide under sufficient light intensity and ambient temperature. In a single real-world thermal cycle, our design triggered 142 activations of a self-oscillating actuator, while a two-limbed soft pneumatic robot harvested thermal energy to achieve locomotion. This study presents a long-term energy-harvesting strategy enabling energy autonomy in electronic-free soft robots without repeated manual intervention.

Soft robots have gained popularity as a result of their intrinsically adaptable interaction with their environment[1,2]. This feature has motivated the widespread exploration to use soft robotics in, e.g., medicine[3], chemically or mechanically hazardous environments[4,5], and in the food industry[6,7]. Their application in these often unstructured and unknown environments can become even more appealing when these soft systems can manifest increasing levels of control and energy autonomy, to reduce the need for human intervention and (tele) operated supervision. While recent studies have shown that soft robots can navigate complex environments or change their actuation pattern based on external stimuli[8–10] with no need for humans in the control loop[11,12], solutions to combine the harvesting, storing and control of the energy necessary to power these systems are lacking.

Most soft robots depend on the use of tethers to provide electrical or pneumatic power[13–15], use wirelessly provided electromagnetic[16,17], acoustic[18] or thermal[19] fields, or harness embedded single-use energy reservoirs (chemical or pneumatic)[18,20–22]. Such powering strategies often require external human interaction with the robotic system or limit their application to specifically controlled environments, thus preventing them from achieving operational autonomy[23]. To obtain autonomous systems capable of continuous operation, the idea of harvesting energy from naturally occurring environmental changes, e.g., in light intensity and temperatures, to power responsive machines has been explored[24–30], with only a few examples working on strategies to enable energy autonomy[31–33]. Similar principles have recently been investigated in the context of architectures with embedded electronics-free control, actuation, and powering for smart building façades[24]. However, for these and similar studies, the incoming energy is directly used by the actuators to power automatic responses, rather than a more versatile strategy in which harvesting, storing, and controlling the use of the gathered energy can be separated in time.

[1]Autonomous Matter Department, AMOLF, Amsterdam, The Netherlands. [2]Institute for Complex Molecular Systems and Department of Mechanical Engineering, Eindhoven University of Technology, Eindhoven, The Netherlands. e-mail: j.t.b.overvelde@tue.nl

In the present work, we propose a strategy to achieve energy autonomy in pneumatic soft robots. Inspired by the view of ref. 34, our approach aims towards the integration of control, power, and actuation components within the same bodyware of soft robots intrinsically designed to operate in natural environments. Here, we design a thermopneumatic cycle that can slowly harvest thermal energy from the environment and store it as pneumatic pressure, after which it can be discharged more quickly to power and control soft pneumatic devices. The heat engine cycle is designed around naturally occurring environmental oscillations of temperature and light intensity during the day-night cycle, to enable autonomous energy harvesting during multiple cycles. The term circadian in the title and throughout this work indicates that the system can be powered and actuated by day-night oscillations in temperature and daylight, rather than implying a once-per-day operation. Our approach is based on the pressure generated by the evaporation of a Low-Boiling-point Fluid (LBF), which we couple to a hysteretic valve for controlled pressure release. Compared to previous work that mainly achieved direct responsive systems[31,35–40], the use of such a hysteretic component is essential to decouple harvesting and release of energy.

We first present our concept for a thermopneumatic cell that can repeatedly harvest, store and release energy obtained from the environment. We evaluate the performance of our system using experiments performed in a controlled lab environment. Secondly, and based on our experimental observations and thermodynamic understanding, we develop a lumped thermodynamic model to simulate the pneumatic response and energy harvesting capabilities of our approach in different locations worldwide. Finally, we show the potential for applications in the context of pneumatic soft robots by demonstrating the operation of our energy-harvesting cell in an outdoor environment. Moreover, we embed our thermopneumatic circuit in a locomoting soft robot to show that our design can be integrated and used as an on-board energy-harvesting element.

Results

Thermopneumatic design concept

We extract thermal energy from the environment through a thermopneumatic cell that is driven by the evaporation and condensation of an LBF (Novec 7000®, $T_{boil}(p_{amb}) = 34$ °C). Evaporation of Novec 7000® has been successfully used in other soft robotics studies, where actuation is achieved by artificially controlling the temperature using heat sources from resistive heating elements to acoustic waves[39,41–43]. Here, our goal is to use naturally occurring temperature and solar intensity oscillations during the day-night cycle to harvest, store, and use energy from the environment. The thermopneumatic design concept we use to materialize these functionalities is shown in Fig. 1a, where we distinguish between (*i*) the component to harvest and store pneumatic energy, (*ii*) the component to control the pressure release, and (*iii*) the component that uses the pressure to perform some function and to do work.

Harvesting and storing pneumatic energy. To harvest thermal energy from the environment and store pneumatic pressure, we insert a pouch of 15 cm by 19 cm of heat-sealed nylon coated with TPU containing 5g of LBF inside a 1L plastic bottle that operates as a stiff air reservoir. We provide more details of fabrication in the "Methods" section. If we close the container and increase the temperature of the LBF-pouch above its boiling temperature T_{boil}, the LBF undergoes evaporation. As a result, the LBF-pouch expands, compressing the air inside the reservoir. The more thermal energy is added to the system,

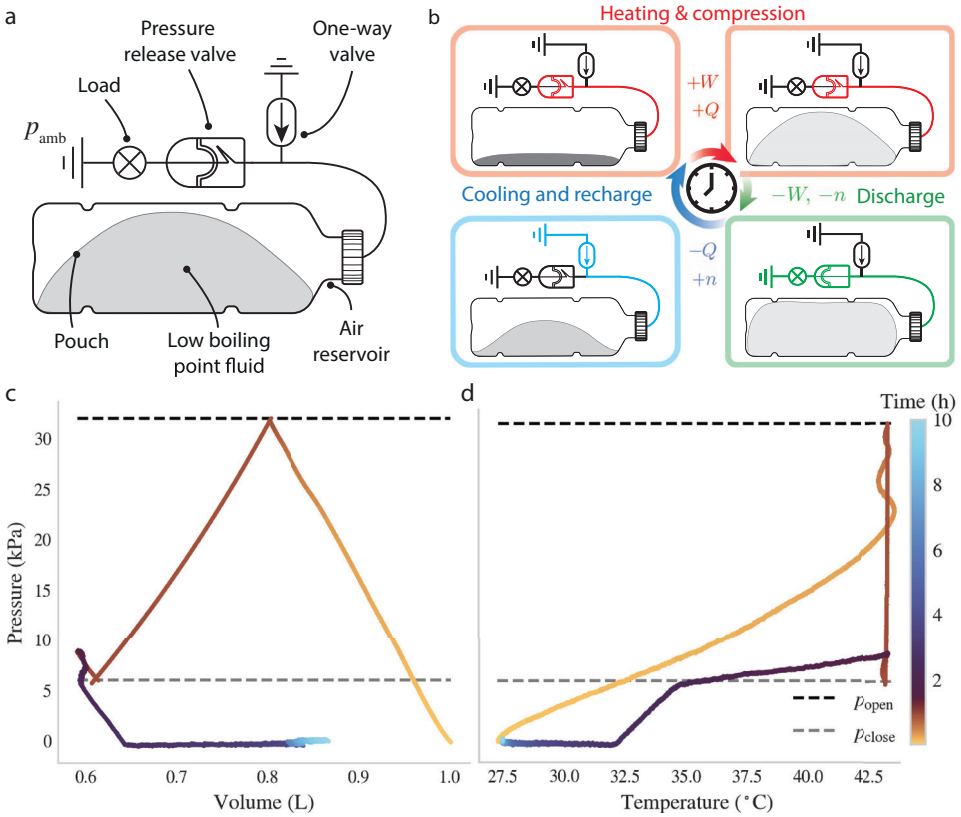

Fig. 1 | Overview of the thermopneumatic harvesting cell and experimental data of energy harvesting cycle. a Thermopneumatic circuit design. **b** Working principle of a single energy harvesting cycle. We distinguish between the compression, discharge, and recharge phases (respectively in red, green, and blue), where we highlight the branch of the pneumatic circuit that is involved in each of the processes together with the state of the pneumatic valves. **c**, **d** Experimental data from the thermopneumatic cell during one thermal cycle from $T_{lab} = 27–43$ °C in 2 h before thermalizing back to T_{lab} in 8 h.

the larger the volume change of the LBF-pouch as a consequence of the vaporization, resulting in a higher internal air pressure in the container.

Note that the use of the LBF-pouch is essential to reach sufficient pressure in the container. While the thermal expansion of the air inside the container also contributes to an increase in pressure, we show through a comparative experiment (SI section A.2) that the maximum pressure reached at a temperature increase of 30 °C differs between ≃ 18 kPa for only air, and ≃ 90 kPa when including the LBF-pouch. This is mostly due to the fact that, as the fluid evaporates, it undergoes a density change of about three orders of magnitude, whereas, in the ideal-gas law regimes we investigate here, the same temperature increases of the air volume alone causes a pressure increase about five times lower. Practically, the use of an LBF-pouch allows us to localize energy harvesting and storage, while the air inside the air reservoir can be exchanged with the outside environment.

Regulating the pressure inside the container. Although we could directly connect the air reservoir to a soft actuator for activation, this directly connects the environmental conditions to the actuator state. This limits the power conversion capabilities as seen in natural systems, which we wish to reproduce[44,45].

Instead, to decouple the timescales of charging and actuation, we connect a custom-made pressure relief valve to the air reservoir as shown in the schematics in Fig. 1a. By decoupling of timescales we mean that, unlike approaches where harvested energy is converted into actuation as it becomes available[25,46], our system stores incoming energy during a slow compression (charging) phase and releases it only after reaching a threshold via a much faster discharge, followed by a distinct recharge process. The working principle of the pressure relief valve is based on a previously proposed—but not yet implemented—design[47], and is based on a monostable elastomeric dome with a silicone tube that passes through the pole of the dome. We provide additional information about the valve design and fluidic properties in the "Methods" sections and in SI section A.5.

This valve has two inlets connected in parallel, one connected to the silicone tube and the other connected to the chamber enclosed by the dome itself. The opposite end of the silicone tube is used as the valve outlet. In the resting (normally closed) state, the input pressure p is lower than the activation pressure p_{open}, and the dome kinks the silicone tube, preventing the flow of air. When $p > p_{open}$, the elastomeric dome snaps and unkinks the silicone tube that passes through its pole, allowing the air to flow through the tube. The valve remains in the open state until p drops below p_{close}, the pressure at which the dome transitions back to its monostable state. When this condition is met, the silicone tube kinks again and the valve transitions back to the closed state. Note that given the relatively long time scales involved in the thermopneumatic cycle, it is essential that the valve does not leak. We found that similar valves often show leakage that, although typically relatively small, makes them unsuitable for this specific application[48].

In our thermopneumatic design, the amount of LBF, together with the pressure-release valve critical pressures, fully determines the kind of load that can operate downstream to the energy harvesting cell. As we measure in a comparative experiment in SI section A.2, by increasing the amount of LBF, it is possible to achieve higher pressures upon vaporization. At the same time, by modifying the geometry of the pressure-release valve and thus its opening pressure (SI section A.5), we can achieve a greater energy buildup in the energy harvesting cell.

In addition to the pressure relief valve, we also add a commercial one-way valve in parallel to the pressure relief valve (Fig. 1a). This one-way valve ensures that outside air can flow back into the container when the pressure inside the container drops below the atmospheric pressure. This is essential to refill and restore the system to the initial conditions after every activation cycle.

Thermopneumatic cycles: harvesting thermal energy to perform work. Now that we have a way to harvest thermal energy, store pressure, and control the release, we focus on the resulting thermopneumatic cycle that the system undergoes to perform work when subjected to an increase and decrease of temperature. Before connecting more complex fluidic circuits or actuators after the pressure relief valve that can power soft devices and robots, we first connect a resistive load to gain more insight into the behavior of the developed thermopneumatic system.

The thermopneumatic cycle for our system can be defined in three phases as indicated in Fig. 1b: the heating & compression phase, discharge phase, and cooling & recharge phase. We can observe these phases experimentally when connecting our device to the resistive load (Fig. 1a) and placing it in an oven (Memmert®UF30plus) that regulates the temperature from T_{lab} = 27 to 43 °C for 2 h, before letting it cool back to T_{lab} for 8 h. Without loss of generality, when discussing the temperature T in our experiments, we refer to the temperature of the air inside the air reservoir as in Fig. S18a, unless stated otherwise. Figure 1c, d reports the pressure, volume, and temperature of the air inside the air reservoir resulting from a single thermal load cycle. The heating & compression phase is defined as the period during which pressure builds up as a result of increasing temperature and evaporation of the LBF. As the internal pressure increases from 0 to 32 kPa, the LBF-pouch expands, causing the geometric volume of air in the container to decrease. Note that if no LBF-pouch had been present, the geometric volume V of the container would not change, and the volume V would remain 1 L. Therefore, we can infer the geometric volume of the LBF-pouch from Fig. 1c, which equals approximately 0.2 L at the end of the heating & compression phase.

This phase transitions into the discharge phase, which is initiated by the opening of the pressure relief valve when $p > p_{open}$, and results in the release of air from the container through the pressure relief valve. As a result of the discharge, the pressure of the air inside the container drops, causing the LBF-pouch to further expand and act as a pump to drive additional air out of the container. This process occurs until $p < p_{close}$ and the TPU pouch occupies about 0.4 L of the geometrical volume inside the rigid container. Note that after the valve closes, the pressure inside the container can increase again if more heat is provided to the system, as can be seen by the small increase in pressure at the end of the discharge phase. This is a result of the decoupling of time scales.

Finally, the cooling & recharge phase is initiated when the applied temperature starts to decrease, resulting in the condensation of the LBF that leads to a decrease in the LBF-pouch volume. This effectively generates a negative pressure in the air container when reaching 32.5 °C (Fig. 1d), which initiates air flow through the one-way valve to (slowly) restore the air volume in the reservoir. As such, the environment around the energy harvesting unit operates as a pressure regulator at ambient pressure during this phase.

Note that in Fig. 1c, we do not measure a full reset to the initial conditions of the thermopneumatic loop after a single controlled thermal oscillation. Conversely, in a comparative experiment (SI section A.3), we show that our system has the potential to recover its initial conditions and that the discrepancy between the initial and final geometrical volume of air lies mostly in the non-zero closing pressure of the commercial pressure-release valve. Although we acknowledge the possibility of leakages of LBF through the TPU pouch, we do not reckon leakages of powering fluid to be pronounced enough during the time scale of a single thermopneumatic cycle to prevent the full recovery of the initial conditions.

Performance of our thermopneumatic cycle

From a single thermopneumatic cycle, we can extract the energy output harvested from the environment. Integrating the pressure-volume data in Fig. 1c, we obtain that a single thermal cycle has

https://doi.org/10.1038/s41467-026-77422-2

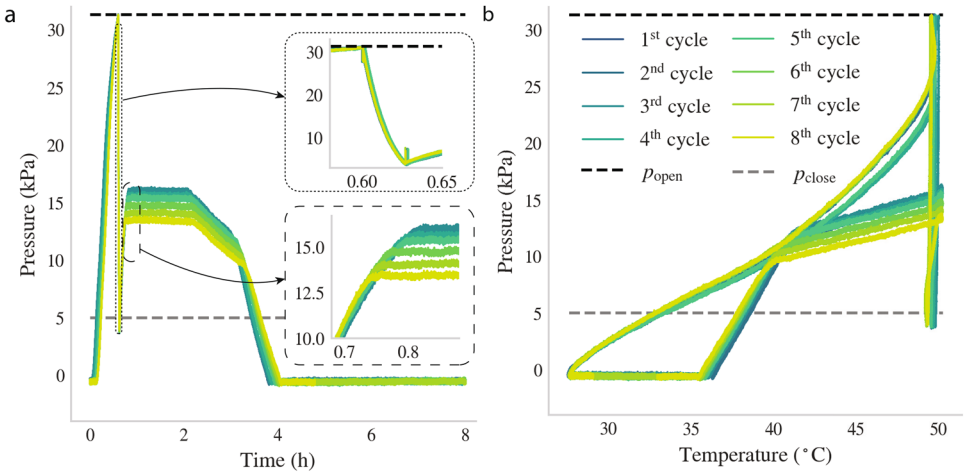

Fig. 2 | Experimental data for continuous repeated charging and discharging of the energy harvesting cell. We place the thermopneumatic cell in an environment where we control the temperature. We obtain eight continuous loops of thermal oscillation, in which we bring the temperature from T_{lab} to 50 °C in 2 h, before letting the system thermalize back to T_{lab} in 6 h. **a** Pressure in time during to the discharge phase (dotted) and saturation after the discharge phase of the heating provided to the system. **b** Pressure-temperature plot of the same data as in (**a**) for the repeated cycles.

approximately dissipated 6J of energy through the resistive load. This energy can be defined as the work done by the system in this specific scenario. Assuming that the system is back to its initial state at the end of the cycle, the same amount of thermal energy has thus been harvested from the environment. While this number seems relatively low, we will show later that it is sufficient to power an untethered robot. Moreover, the harvested energy is significant compared to the maximum energy stored in the system at any time, which we estimate to be close to $\Delta p \cdot V \approx 30\,\text{kPa} \cdot 1\text{L} = 30\,\text{J}$. Specifically, if we assume an ideal case where all the air molecules inside the air reservoir are expelled throughout the discharge phase and by using an ideal pressure-release valve with the same Δp_{open} but a $\Delta p_{close} = 0$ kPa, a maximum value of about 15 J could be harvested.

We can furthermore derive the efficiency of transforming thermal energy (heat) into mechanical energy (pressure) to be equal to $\eta = 0.87\%$, which can be compared to an ideal Carnot cycle that would give an efficiency of $\eta_{Carnot} = 5.06\%$ (see SI section A.6 for details). For a better comparison, we consider engines that rely on phase transitions like the ones we base our energy harvesting device on, such as Organic Rankine (OR) engines, rather than on chemical reactions such as Otto or Diesel engines. In the case of OR engines, we observe an efficiency of $\eta_{OR} \simeq 10\%$[49] and $\eta_{Carnot,\,OR} \in [50\% \div 80\%]$ depending on the specific technology considered. When we take into account already optimized technologies, such as OR engines as a reference, it seems that for the thermopneumatic cell, we reach η/η_{Carnot} in the same order of magnitude as OR engines. In addition, for our case study, we measure a specific energy density of $\approx 112.6\,\frac{\text{J}}{\text{kg}}$ and a specific power density of $\approx 2.7\,\frac{\text{W}}{\text{kg}}$.

It should be noted that when we compare the performances of the thermopneumatic device over other commonly investigated methods for energy autonomy in terms of specific energy density, specific power density and efficiency (Fig. S7, we find that our approach offers comparable quantities compared to previous work based on chemical reactors. Yet, it is important to mention that previous research investigating energy autonomy focuses primarily on energy regulation rather than energy harvesting[23], and therefore needs to be (manually) refilled after every use. The fact that our system can harvest energy from circadian cycles is a characteristic feature of energy-autonomous systems. Therefore, when comparing our specific energy and power density to other systems, the numerical values must be interpreted carefully by also considering the fundamental differences, capabilities, and purposes between our system and those referenced in the literature.

Repeated energy harvesting cycles

One crucial feature of our energy harvesting approach is that it allows for several cycles of energy harvesting, provided that the temperature oscillations have a sufficiently large amplitude and period. Therefore, we experimentally measure the response of our energy harvesting unit for eight consecutive temperature oscillation cycles. For each thermal oscillation, we increase the temperature from $T_{lab} \approx 27$–50 °C for two hours, before letting the system cool down back to T_{lab} during another six hours. While a temperature of 43 °C should be sufficient to trigger the discharge phase, to ensure that the valve would open up several times during our longer continuous experiment, we imposed a maximum temperature of 50 °C. The results of this cyclic experiment are reported in Fig. 2, where we show the response in the pressure-time and pressure-temperature space.

We find that for all eight cycles, our proposed system is capable of harvesting energy from the environment, and every cycle is approximately identical. Nevertheless, we do measure a non-negligible drift between each cycle, which can be seen by the reduction of the pressure after the discharge phase when the temperature is still at 50 °C. We hypothesize that this drift upon repeated actuation could be caused partly by potential leakages of LBF through the nylon-coated TPU, but predominantly by the non-zero closing pressure of the commercial one-way valve. These two experimental limitations, combined, could cause a decrease in both the powering and actuating fluid that generates the pressure shift after the discharge phase. This statement is supported by analyzing the data further, where the results in SI section A.4 show that the decrease in pressure after every cycle stabilizes at ≈ -0.6 kPa after the fifth cycle.

Modeling the harvesting response to real-world conditions

The experiments and resulting analysis we performed so far took place in lab conditions, only taking into account changes in ambient temperature. Therefore, in this section, we model the response of the design of the energy harvesting unit under more realistic real-world conditions. We start by leveraging the previous experimental results to build a model, after which we inform it with historical data from weather stations.

https://doi.org/10.1038/s41467-026-77422-2

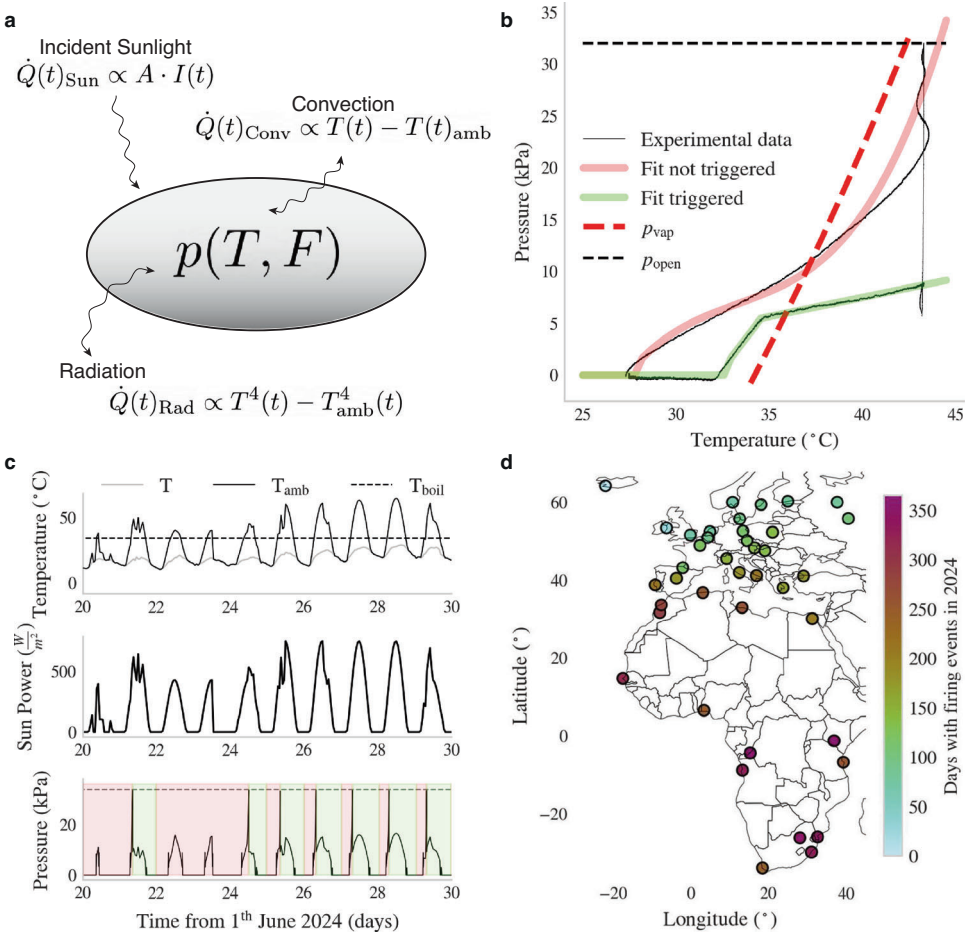

Fig. 3 | Results for modeling the behavior of the energy harvesting cell. a Gray-box model of the thermopneumatic cell of heat transfer, including convection, radiation, and incident sunlight. **b** Fits of experimental data in the pressure-temperature space when the pressure-release valve has (in red) and has not (in green) been triggered. We report the vapor pressure of the LBF with the dashed red line. **c** Ambient (gray) and simulated air (black) temperature, simulated absorbed sun power on the thermopneumatic unit area, and simulated pressure inside the unit throughout the first two weeks of June 2024 in Amsterdam. We highlight whether a firing event occurs during the specified time window in green and red, respectively. **d** Simulated number of days with a firing event for 2024 in different locations between −20° and 50° longitude.

Modeling the temperature in the reservoir. Phase transitions with simultaneous changes of volume, temperature, and pressures results in polytropic non-quasistatic thermodynamic processes that are non-trivial to model. Furthermore, a thermopneumatic model capable of predicting the response of the energy harvesting cell should also be able to account for different slow time scales (compression and recharge phases) as well as the fast time scale (discharge phase) simultaneously. As we want our model to predict the response of our thermopneumatic cell in real-life conditions, we should not only consider the thermal response as observed in the previous experiments performed in lab conditions, but also incorporate contributions from light intensity and radiative heat transfer.

Combining these considerations while keeping the focus on the energy harvesting applications for pneumatic soft robots, we derive a physics-based lumped model starting from fundamental thermodynamic heat exchange rates $\dot{Q}$ as shown in Fig. 3a, and described in detail in the SI section B. We assume that the temperature $T(t)$ in the reservoir and pouch are identical, where the temperature change depends on contributions from radiation, convection and absorption. Moreover, as a first approximation and to simplify the model, we assume that the pressure inside the reservoir does not influence the thermal properties of the cell.

The result is a model where the temperature evolution can be determined by specifying the initial temperature $T(0)$, the ambient temperature T_{amb} and incoming sun radiation $I(t)$. All other parameters can be derived from existing literature, with the only exception being the geometrical coefficient α that accounts for the effect the position of the sun has on absorption. We describe in the SI section B how we used experiments to fit this quantity.

Modeling the pressure in the reservoir. Although the introduced model allows us to determine the temperature, predicting the pressure $p(t)$ in the reservoir of the pneumatic cell requires us to know the current state of the system. We define a Boolean variable F that best indicates the current state of the system. When F is False, the system has been fully recharged to ambient conditions and is ready to harvest energy from its environment. In contrast, when F is True, the system has reached the critical pressure to open the pressure relief valve, discharged its pressure, and should be recharged. Based on the state the system is in, the pressure in the energy harvesting cell can follow two different paths in the pressure-temperature plane, as observed in our experimental data from Fig. 1d.

Let us first focus on the case for which F is False. For $T > 27$ °C, we measure a continuous increase in air pressure as indicated by the fit in Fig. 3b. Considering the boiling temperature of the LBF at a given pressure $T_{\text{vap}}(p)$ and the scaling of vapor pressure $p_{\text{vap}}(T)$ of the LBF with changing temperature, as T increases, we assume the vapor pressure increases following the Clausius–Clapeyron equation (Eq. (S1)

https://doi.org/10.1038/s41467-026-77422-2

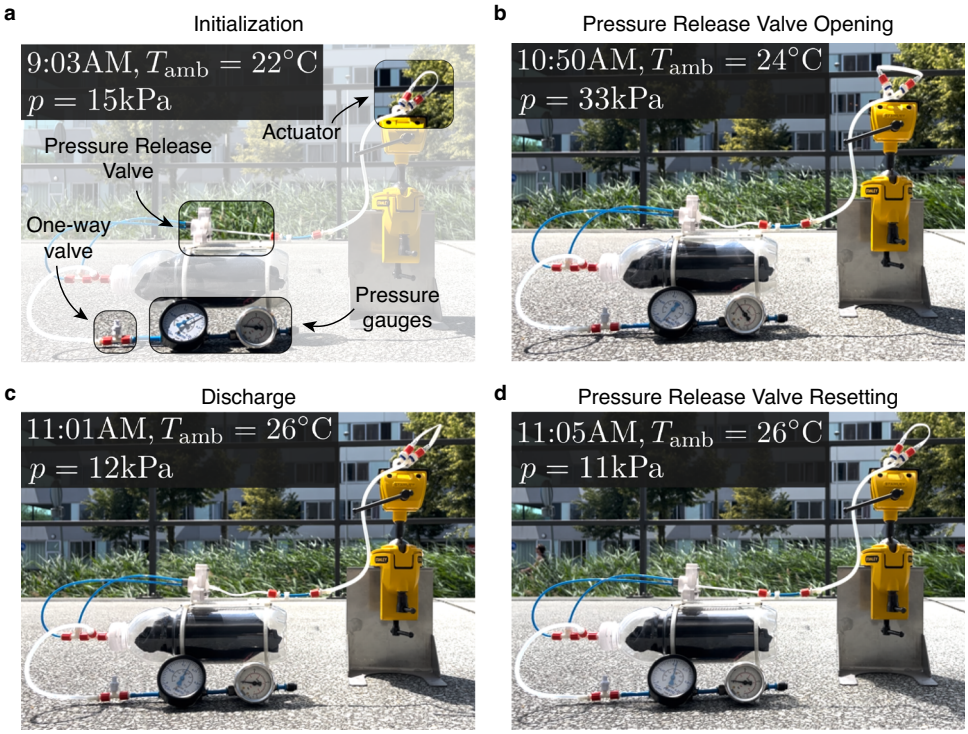

Fig. 4 | Snapshots of an outdoor experiment where we harvest thermal energy to power a self-oscillating actuator. a Initialization of the system with highlights of the main components. **b** When $p = \Delta p_{open} = 33$ kPa, the pressure-release valve opens, and the self-oscillating tube actuator starts to perform its motion. **c** The actuation lasts throughout most of the discharge phase, while the total pressure inside the air reservoir drops. **d** As $p = \Delta p_{close} = 11$ kPa, the valve transitions back to its closing state. The pneumatic circuit of this demonstrator is the same as in Fig. 1a, and for comparison also shown in Fig. S18a.

in SI section A.1). This also accounts for an increasing boiling temperature as a result of increasing pressure, which is more significant when pressures inside the air reservoir are higher.

Next, we consider the case for which F is True. After a firing event of the valve, we observe a discontinuous $p(T)$ with three distinct linear regimes. When $T > T_{vap}(p)$, variations in environmental temperature cause linear changes in pressure that we explain by considering the ideal gas law on both the remainder of the air inside the air reservoir after the discharge phase, as well as the LBF in the gas phase. Instead, when the $T \simeq T_{vap}(p)$, condensation of the LBF occurs. Consequently, we observe a sudden change in slope in the pressure-temperature plane due to the reducing volume of the TPU pouch, up until most of the LBF transitions back to its liquid phase. This decrease in pressure continues until reaching pressures close to the ambient pressure, where it is mainted at $p_{amb}-\Delta p_{open,1way}$ as a result of the slow recharging of the reservoir through the one-way valve.

For completeness, we report $p_{vap}(T)$ using the fit suggested from the technical datasheet of the LBF (Eq. (S2) from SI section A.2) in Fig. 3b. The small deviation we observe between the $p_{vap}(T)$ curve and experimental data can be explained by considering that the vapor pressure is measured with LBF alone, while we measure the response of the whole thermopneumatic system.

Finally, we consider when the system changes the state F. In our model, we switch F from False to True whenever $p \geq \Delta p_{open}$. Moreover, based on preliminary experimental trials, we observe that it takes about 6 h to complete the recharge phase. Thus, we assume the recharge phase to be fully completed if the temperature drops below 27 °C for at least 6 h, switching back F from True to False. Although this approximation is quite conservative in terms of the modeling of the recharge capabilities of the energy harvesting cell, directly modeling the amount of change in the number of air molecules in the air reservoir during the recharge phase proves to be a non-trivial task.

Note that during recharging, we observe that when the temperature inside the air reservoir T is lower than 27 °C, the air pressure inside the air reservoir is $p(T \leq 27\,°C) = p_{amb}-\Delta p_{open,1way}$. Here, $\Delta p_{open,1way} \simeq 1$ kPa is the opening pressure of the one-way valve triggered during the recharge phase. When the air reservoir has completed the recharge phase, we measure $p = p_{amb}-\Delta p_{close,1way}$ with $\Delta p_{close,1way} \simeq 1$ kPa is the opening pressure of the one-way valve.

Simulating real-world conditions. The lumped model now allows us to coarsely predict the behavior of the thermopneumatic cell under real-world conditions. To do so, we use weather station data for different coordinates to simulate the pressure $p(T, F)$ in the reservoir, as a function of ambient temperature and sun intensity at different locations and times around the world. First, in Fig. 3c, we show an example output of the pressure $p(T, F)$ in our simulated environment for the last days of June 2024 in Amsterdam. Based on the ambient temperature T_{amb} and sun power intensity I gathered from weather station data, we simulated the air temperature T_{air} inside the energy harvesting cell.

From our simulated data, it is apparent that a firing event can occur even if the ambient temperature T_{amb} is lower than T_{boil}. This is mostly due to the presence of sunlight intensity and indicates the importance of sunlight in the heat transfer balance. From the same data, we also observe abrupt changes in incoming solar power resulting from the presence of cloud coverage. We observe that even if T_{amb} does not dramatically change between the days in Fig. 3c, cloud coverage can hinder heat transfer contributions from solar radiation and prevent firing events. Our model also includes the effects of air moisture on specific heat capacity, although we observe that air moisture has only a marginal effect on the results. We report an extended explanation of our model in Supplementary Material B and Eq. S15, where we also provide an in-depth explanation on the effect of wind to the heat transfer mechanisms.

https://doi.org/10.1038/s41467-026-77422-2

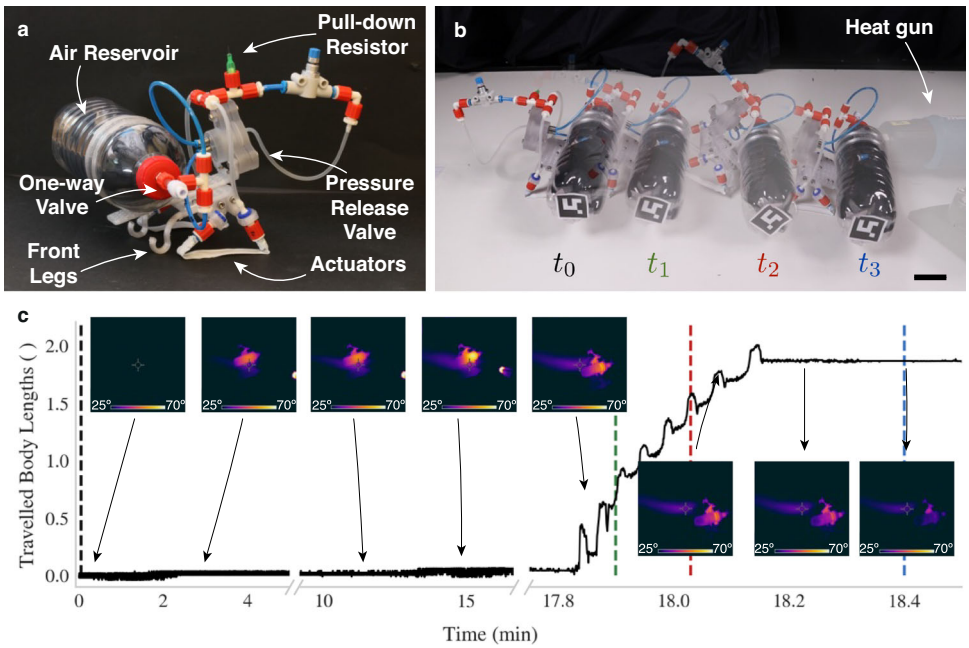

Fig. 5 | Energy autonomy of a soft walker demonstrated in laboratory environment. a Schematics of the main hardware components of an untethered walker powered by an energy harvesting cell. **b** Overlay of snapshots during the locomotion phase. Once the unit starts to locomote, the thermal source (heat gun) is moved away from the walker's trajectory to avoid heat damage to its components. The scale bar represents 5 cm length. **c** We track the walker's position using a fiducial marker on the side of the air reservoir and plot the unit position in time. At the same time, we gather information about the walker's temperature using an IR camera in the insets at the corresponding highlighted timestamps. We report the pneumatic circuits of this demonstrator in Fig. S18b.

We next simulate the response of the energy harvesting cell using data from 2024 at different locations. In Fig. 3d, we report the predicted total number of days during 2024 for which the cell would have fired, for different locations in Europe and Africa. It is apparent that there is a correlation between latitude and the total number of observed firing events during the year. Yet, we do observe variations for locations with similar latitudes, which are mostly due to the local orography and nearby water masses, as also demonstrated in Fig. 3d when comparing, e.g., Bilbao to Rome. We interpret the number of firing events during a full year as a quality factor for the simulated performance of our thermopneumatic energy harvesting strategy, aware that the representation in our lumped model of the recharge phase is highly simplified.

Demonstrators

With the goal in mind to probe the potential for applications of our energy harvesting cell, we target soft robotics applications by testing the capability of our thermopneumatic approach in two separate settings. In the first demonstrator, we evaluate whether real-world conditions can be sufficient to trigger the compression and discharge phases in our thermopneumatic strategy by leaving our electronics-free design in real-world conditions outside of the lab. In addition, we aim to use the released pressure to power a self-oscillating soft actuator. In the second demonstrator, we aim to evaluate if the thermopneumatic cycle generates sufficient energy to power the locomotion of an untethered walking soft robot that uses two self-oscillating limbs to propel itself forward.

Compression and discharge phases in a real-world environment. In the first demonstrator, we place the energy harvesting cell from Fig. 1a in an outdoor environment for 2.5 h, while measuring its pressure in time as the system is subjected to both temperature increase and incident sun radiation (on June 27th 2024 in Amsterdam). To demonstrate the advantages of decoupling the charging and discharging time-scales of our thermopneumatic cell, in this experiment, we replace the fluidic resistor with a self-oscillating tube actuator[50]. The tube actuator manifests self-oscillating behavior (at frequencies $\in$ [1, 4]Hz) when subjected to an inflow greater than 0.1SLPM and a pressure greater than 10kPa. By separating the timescales between energy harversting and actuation, combined with a relative low pressure and air flow activation thresholds for the self-oscillating actuator, the setup should guarantee that a single energy harvesting event can return a relatively large number of activations of the actuator (see "Methods" sections).

To perform our experiment, we first initialize the system at laboratory conditions of $p = p_{amb}$ and $T_{lab} = 27\,°C$ and then bring it to the outside environment, exposed to sunlight as in Supplementary Movie 1 and Fig. 4a. During this experiment, as expected, we observe a gradual increase in pressure during the compression phase up until the discharge phase occurs at $p \simeq 33$ kPa (Fig. 4b), as indicated by the analog pressure sensors.

Throughout the discharge phase, the pressure triggers the self-oscillating actuator to start oscillating, which causes the pressure to decrease slightly after every activation cycle (Fig. 4c). This discharge phase lasts for about 15 min, where we observe a total of 142 oscillations of the actuator, after which the pressure-release valve automatically transitions back to its closed state once the air reservoir hits the closing pressure of the valve at $p \simeq 11$ kPa (Fig. 4d). During this experiment, we observe that actuation frequencies range from 5 Hz, at the beginning of the discharge phase up to 0.1 Hz at the end of the discharge phase. Such a frequency shift is a direct consequence of the drop in driving pressure and flow as the self-oscillating actuator operates as a resistive load.

By comparing the approximate energy cost for a single oscillation in the self-oscillating tube actuator of 0.06 J[50] to the energy that we harvest from a single circadian oscillation ($\simeq$ 6 J) from the pressure-volume curve in Fig. 1c, we can derive that a single energy harvesting cycle should generate approximately 120 activations of our actuator. This prediction is close to the observed 142 oscillations, suggesting that our approximation of the harvested energy from our

thermopneumatic device is in the same order of magnitude as the one we observed. In particular, with this demonstrator, we show that the separation of time scales, combined with the relatively low amount of energy required for each activation of the self-oscillating actuator, is sufficient to repeatedly generate motion with a single discharge phase from the energy harvesting unit. Moreover, although not directly evaluated here, we mention that under sufficiently high environmental temperature and solar irradiance, the system may undergo multiple actuations within a single day, with successive compression-discharge events occurring without an intervening recharge phase. Continued heat influx has potential for triggering a secondary firing, which can enhance vacuum generation during recharge but yields reduced mechanical work due to the smaller displaced air volume.

Harnessing heat from the environment to generate locomotion. In the second demonstrator, we aim to show the potential for energy, control, and actuation autonomy through our thermopneumatic approach. To that end, we design an untethered walker powered by our energy harvesting cell. Based on a similar soft-legged robot design that we introduced while developing control-autonomous walkers using self-oscillating tube actuators[50], we 3D print PETG hardware components to connect all parts of the soft-legged robot. In this demonstrator, we assemble the same thermopneumatic circuit schematic as the one we investigated in Figs. 1a and 4, but use a PET bottle with 0.5 L volume, while keeping 5g of LBF inside the same TPU volume. This choice was made to make the size, mass, and moment of inertia of this walker more compatible with the forces expressed by the actuators. The final soft-legged robots weighs 154g (out of which 82g for the pressure-release valve) and we report the schematics of the walker design in Fig. 5a, together with further details on the specific pneumatic circuit in the "Methods" section.

As the oven previously used is too small for the soft-legged robot, we instead use a heat gun set to 220 °C, positioned at about 30 cm from our demonstrator, to simulate incoming environmental heat and provide sufficient heat to drive the thermopneumatic cycle. We found that this relatively high temperature is necessary for the system to stabilize at about 50 °C for long enough to evaporate the LBF and pressurize the air past Δp_{open}, given the temperature (T_{lab} = 27 °C) and volume of the room (12 m^3) where the experiment was performed. After heating the system for ≈ 18 min, the pressure-release valve opens, and the pressurized air discharges through the actuators. The force exerted by the pressurized air causes the self-oscillating actuators to activate synchronously, pivoting the robot on its rigid front legs and allowing it to progress forward, as we show in Supplementary Movie 2 and Fig. 5b. Even though the experiment successfully demonstrates eight activation cycles, the locomotion phase takes place only during the first part of the discharge phase. This is likely because there is a threshold force needed to be exerted by the actuators to tilt the body of the walker and initiate locomotion.

During this experiment, we measure the robot's position using an ArUco fiducial marker as shown in Fig. 5c, indicating that the robot moved a total of 2 body lengths (i.e., 40 cm) during the activation event. At the same time, we visualize the temperature of the walking unit using an infrared camera to get better insights into the heating and cooling time scales, given the imposed environmental conditions. We estimate the cost of transport (COT) of the walking demonstrator from the cycle energy E = 6 J, system mass m = 0.154 kg, gravitational acceleration g = 9.81 m/s^{-2}, and travelled distance d = 0.4 m. Based on these values, we obtain a COT = $E/mgd \approx 10$. This value is comparable to a previous walker using the same actuators (COT ≃ 11 in ref. 50) and falls within the range reported in locomotion-focused studies (COT ≃ 4.8 in ref. 51 and COT ≃ 30–67 in ref. 52). Although our locomotion duration is shorter and has a lower speed as a result of the design, our approach demonstrates that one important avenue to increase the COT is by harvesting energy directly from the environment as we do not have to consider conversions from, e.g., battery to pumps.

To further illustrate that environmental conditions can cause the soft-legged robot to trigger multiple times, in Supplementary Movie 2, we report the same experimental setup as the one in Fig. 5 with the system experiencing two consecutive cycles of compression, discharge (locomotion), and recharge phases.

Discussion

In this work, we proposed and investigated a strategy to materialize energy harvesting capabilities in soft pneumatic systems. By leveraging fluidic and mechanical nonlinearities, we demonstrated that thermopneumatic cycles can decouple the time scales of energy harvesting and storage. As a result, our approach enables the accumulation of sufficient environmental energy to generate the air flows and pressures compatible with the operation of soft robotic systems. The modelling efforts we have developed in this present work are meant to corroborate intuitions on the design principles for prototyping systems based on a thermopneumatic approach rather than providing quantitative justification of specific parameters. Nevertheless, through our modelling efforts, we demonstrate that parameters such as critical pressures, vapor-pressure curves, together with thermodynamics and pneumatic networks parameters, become design parameters to tune for targeting specific applications. We believe that, although not supported by additional physical experiments, our in-silico efforts can still have potential to address future research questions that may stem from our work.

Our results highlight two key features for materializing energy harvesting in soft robotic systems, with no human-in-the-loop required for their autonomous operation. First, the system must return to the same state at the beginning of each circadian cycle, specifically in terms of thermodynamic variables and mass of powering and actuating fluids, to guarantee repeated, unsupervised operation. At the same time, the energy harvesting unit we design should be able to release the accumulated energy to enable operation on a timescale quicker than the circadian oscillations, instead of providing a slow continuous response throughout the single harvesting cycle. Moreover, we demonstrate that our proposed system operates simultaneously as an energy harvesting and energy storage unit. Autonomous entities in nature also often implement both requirements[53], from the ballistic ejection of spores and seeds in fungi[54], plants[55], and prey capture in both terrestrial and marine animals[56,57]. Similarly, we require that such energy autonomous systems should be capable of decoupling of power conversion, with a slow time scale for energy harvesting and a faster one for operation in their environment.

While we focused on the design of a thermodynamic process for the energy harvesting unit and its potential use for soft robotics, further optimization should be done to be able to implement our approach reliably in real-world applications. For example, we observe a slow, yet consistent, decrease in energy being harvested for repeated cycles. Still, our measured efficiency lies within the same order of magnitude as the Carnot efficiency for our system and is comparable with the efficiency of technologies known in literature, such as Rankine engines.

We believe that our strategy can add an increased level of programmability to early examples working in this direction, such as temperature-responsive shape morphing systems[58], smart façades[59], and biobased, stimuli-responsive robots[60]. We envision potential improvements to our thermopneumatic strategy that can pave the way toward outdoor applications. For example, working with lower threshold opening pressures on the pressure-release valve or multiple buffer volumes as an air reservoir could allow, e.g., multiple firing events during a single day, or not waste the work done to pressurize air inside the air reservoir even if a firing event is not triggered. Furthermore, using the combined effect of temperature differences and

incident sunlight could be more beneficial than relying exclusively on solar or thermal energy-based systems alone.

On top of that, while a more absorbing pouch material would likely increase light-to-heat conversion, we did not yet consider alternatives that are compatible with our fabrication constraints and required material properties. Beyond material changes, we envision the integration of passive self-oscillatory mechanisms (e.g., self-shadowing and self-focusing[61–63]) as a strategy to enhance heating during compression while reducing exposure during discharge/recharge, thereby accelerating recovery and potentially increasing cycle frequency.

In addition to soft robotics applications, we foresee our approach could facilitate tasks of already existing technologies by introducing redundant, electronics-free, and reliable hardware-based solutions for sustainable energy harvesting. Although locomotion and manipulation remain common benchmarks in soft robotics, we believe our thermopneumatic approach can be used in different endeavors, e.g., where daily cycles of actuation can be driven by environmental conditions. For example, we believe that the thermopneumatic strategies we presented here can be integrated into architectural applications, such as in passive, energy autonomous structures for moving façade in the architecture domain[64,65]. The model we developed can be leveraged to quantify the potential for applications in such and similar case studies in different locations.

Methods

TPU pouch fabrication

To make pouches containing LBF fluid, we heat-seal two sheets of nylon (70 den, one side coated with TPU, 170g/sqm), sealing them at 270 °C using a custom modified 3D printer[66]. The pouch design is based on the sketch in Fig. S11. After trimming the remainder of the material from the heat-sealed pouch, we place a FESTO® 6 tube in the opening and heat-sealing it to the TPU pouch[66]. This allows an effective interface to vacuum air and fill the pouch with the LBF before sealing the connection point using a Luer®stopper.

To evaluate the sizing of the pouch, we consider that, within the ranges of pressures investigated in our work, we observe only limited elastic deformation from the nylon-coated TPU, and thus it can be considered as an inextensible textile. As we expect, the maximum geometrical volume that the pouch can occupy is directly related to the 1 L plastic volume bottle. To obtain an ideal volume of the pouch $V_{\text{pouch, max}}$, we use Eq. (1) developed by Robin[67–88], using for the width $w = 160$ mm and height $h = 190$ mm:

$$V_{\text{pouch, max}} = w^3 \left(\frac{h}{\pi w} - 0.142 \cdot \left(1 - 10^{-h/w} \right) \right) \tag{1}$$

As we show in Fig. S11, we include a 13 mm heat-sealed channel in our design to fit a FESTO® 6 mm tube. Moreover, to reduce local stresses along the heat-sealed corners, we replace all sharp corners with a radius of 10 mm.

Handling precautions for Novec 7000

Novec 7000 should be handled in accordance with standard laboratory safety protocols. Although it is non-flammable, chemically stable, and exhibits low acute toxicity, it is a volatile engineered fluid that can cause eye or skin irritation upon direct contact. Novec 7000 is not classified as hazardous according to OSHA Hazard Communication Standard. However, all procedures should be conducted under a chemical fume hood to minimize vapor exposure, due to significant environmental persistence. Appropriate personal protective equipment, including safety goggles, nitrile gloves, and a laboratory coat, is strongly recommended as well. Inhalation of vapors should be avoided, and prolonged exposure should be minimized. The fluid should be stored in tightly sealed containers in a cool, dry environment away from heat sources. Spills should be cleaned promptly using absorbent materials, and waste disposal must comply with institutional guidelines and local regulations. Users are advised to consult the manufacturer's Safety Data Sheet prior to use.

Pressure-release valve fabrication

The custom pressure-release valve we use in our work is based on a design previously suggested[47], yet it has so far not been experimentally evaluated. Its operating mechanism is based on the kinking instability of a silicone tube passing through the pole of a silicone monostable dome (Fig. S12). To fabricate this design, we cast the silicone dome in a 3D printed mold, and directly 3D print the holder to obtain the components with parameters as in Fig. S13. We print the holder and the molds using Veroclear on an Eden260VS, Stratasys® printer. The silicone dome is made made by injection molding Dragon Skin® 30 (Smooth-On®) in the mold, following the steps in Fig. S14. Before injecting the two-component silicone, we spray Mann Ease Release 200® on the molds in Fig. S14a to guarantee a smooth and easy removal of the silicone once it is cured. We apply a first layer of mold release and then wait five minutes before applying a second layer so that the mold release can settle uniformly before starting the injection molding (Fig. S14b). During this step, we inject silicone from one end of the top injection mold while holding the 3D-printed molds vertically to favor the escape of air bubbles from the opposite side. Once the injection step is completed, we rotate the component horizontally so that the silicone inlet and outlet lay at the same height while the silicone cures.

We wait for the silicone to cure for 16 h to obtain the dome as in Fig. S14c. We then post-process the silicone dome by heating it to 60 °C for 2 h. After this step, we proceed by cleaning the tube and dome with isopropanol, and sliding the silicone tube (2.6 mm outer diameter, 0.3 mm wall thickness) inside the opening in the silicone dome. We leave 1 cm tube protruding from the dome opening on the pole end. On the opposite side of the dome, we make sure to use more than 10 cm of silicone tube to allow a versatile interface with the connectors downstream to the pressure-release valve. To bind and seal the connection between the tube and the dome, we apply SilPoxy® on the concave side of the pole of the dome.

Once we obtain the component as shown in Fig. S14d, we assemble it with the Veroclear valve molds (Fig. S13). We slide 2 mm of FESTO® 4 tube at the end of the silicone tube on the concave side of the dome as in Fig. S15a, and slide it on the pin of the holder as in Fig. S15b. This step guarantees a firm connection between the silicone tube and the holder while allowing the silicone tube to be fully kinked when the valve is in the closed state. We then connect the top side and bottom holders using three M4 screws and obtain the pressure-release valve as in Fig. S15c, d. We complete the assembly by using FESTO® 4 QS fittings on the inlet side to allow a pneumatic interface to the inlet of the valve.

Before using the valve in our experiments, we validate that the valve does not leak in its closed state by performing the tests illustrated in Fig. S16.

Protocol to check leakage-free behavior of the pressure-release valve

To validate that our experimental implementation of the pressure-release valve[47] materializes the leakage-free properties we desire for our design, we perform the following measurements. We connect the pressure-release valve to a pressure regulator to impose a linear increase in input pressure p_{in} from 0 to 45 kPa in 20 min before bringing the p_{in} to 0kPa in another 20 min. We continuously repeat these pressurization and depressurization cycles five times and report the output data for pressure and flow in Fig. S16. We report with the black think lines the individual realization of the pressurization and depressurization cycles. At the same time, in the scatter plot, we report the average values of flow as a function of pressure in time. In the inset, we zoom close to the region of low flows to better highlight that, when

the valve is in the closed state and pressurized at $p < \Delta p_{open}$, no airflow is measured until the opening pressure is reached.

Measurement of thermodynamics variables

To measure and infer the thermodynamic variables in our experiments, we use an NI-DAQ USB-6212, National Instruments® board for all the measurements, with sampling rates specified as in Table S1. We use an SSCDRRN015PDAA5, Honeywell® as pressure sensor (±100 kPa range), and a HAFBLF0750C4AX5 (±0.75SLPM) to measure air flow. We connect the sensor following the schematics in Fig. S17a, with the air pressure and airflow measured in parallel and in series with the air reservoir inlet, respectively. Throughout our experiments with controlled temperature, we enclose the air reservoir inside the Memmert® UF30plus oven. While performing our experiments using the oven, we keep the pneumatic circuit and sensors outside the oven at $T_{lab} = 27$ °C and use FESTO® 4 tube to connect them to the air reservoir.

To gather information on the air temperature inside the bottle while connecting the pneumatic circuit to the air reservoir, we pierce the cap of the plastic bottle we use as air reservoir to obtain two separate openings. We then insert the thermal probe (PT100) inside a FESTO® 6 tube and slide it inside one of the openings. At the other opening, we insert a Luer® connector to create a pneumatic interface between the inside and outside of the bottle cap. We then seal the two openings of the cap using SilPoxy®, and wait 12 min for it to cure. The last step in our protocol is to pressurize the closed bottle with the modified cap and validate that we obtained no leakage at the connection.

While performing experiments with temperature regulation, we use a secondary PT100 probe to measure the temperature inside the oven while regulating it to the desired temperatures. By doing so, we obtain simultaneous measurements of air temperature inside and outside the air bottle to calibrate our heat transfer model. Experimentally, we observe only a limited delay between the two measured temperatures. We speculate that this is due to the low mass of the fluids involved and the thin walls of the PET bottle. As an example of data output, in Fig. S17b we report the measured data for pressure and temperature, together with the inferred air volume using Eqs. (4)–(7) (see next sections) for the experiment in Fig. 1c, d. To infer the volume of enclosed air, we perform our calculations using absolute pressures and K.

Inferring air geometrical volume with pneumatically insulated air reservoir. To infer the air volume when the system is pneumatically insulated from the environment, we start from the assumption that during the corresponding thermodynamic process, the number of air molecules in the air reservoir is constant. We consider this assumption to be valid as we measure zero flow at the outlet of the air reservoir, and we preliminarily check for leakages in our setup. Considering the configuration in Fig. 1a, we define n to be the number of air molecules in the system, R as the gas constant, and T_0 and $V_{0,\,air}$ as temperatures and volumes at the beginning of the thermodynamic process. By applying the ideal gas law, we derive:

$$nRT_0 = p_0 V_{0,\,air} \tag{2}$$

When the system reaches a pressure, temperature p, T, we obtain

$$nRT = pV_{air} \tag{3}$$

Thus, as n is conserved, we infer the correspondent geometrical air volume V_{air}

$$V_{air} = \frac{p_0}{p}\frac{T}{T_0}V_0 \tag{4}$$

We consider this first-order approximation to be valid as, at the thermodynamic ranges we investigate, the compressibility factor $Z = \frac{pV}{nRT} \simeq 1$. At the same time, as we know that within our operating pressure regimes, we observe no deformation of the air reservoir, we can approximate V_{LBF} volume of the pouch containing the LBF

$$V_{LBF} = (p, T, n_{LBF}) = V_{reservoir} - V_{air}(p, T, n) \tag{5}$$

While performing our analyses, we considered these equations to be valid whenever the system is pneumatically isolated from the environment. Therefore, we take as starting conditions (p_0, T_0, n) corresponding to the instances where the pressure release (one-way) valve transitions from the open to the closed state up until the one-way (pressure release) valve opens. In particular, this occurs between the recharge and discharge phases and between the discharge and recharge phases.

Although the ideal gas law is meant to be valid on quasistatic processes, we deem Eq. (4) valid under the hypothesis of slow heating and cooling before and after the discharge phase.

Measuring air volume during discharge and recharge processes. We monitor the amount of air molecules and their volume during the discharge and recharge processes using flow sensors. For our experimental investigation, we use a bidirectional flow meter with a maximum range of 0.75SLPM connected in series with the air reservoir inlet. While performing our experiments, we make sure to include a flow constrictor after the output of the pressure-release valve to guarantee that the peak values we register are within the sensor's range. This requirement is not needed on the input of the air reservoir (output of the one-way valve), as the flow during the recharge phase is already within the sensing range, whereas it helps measure the airflow during the discharge phase by reducing its peak value. In the experiments in Figs. 1 and 2, we use a 22G, 12.7 mm SMD® needle.

To infer volume changes starting from flow values, we first convert the SLPM values into the corresponding number of moles per second Δn, knowing that $1\text{SLPM} = .00073386\,\frac{mol}{s}$. We start by assuming the conditions at t_0 reference start time, thermodynamic variables are pressure p_0, temperature T_0 and volume V_0. Thus, we can derive the initial amount of air molecules in the system n_0

$$n_0 = \frac{p_0 V_0}{R T_0} \tag{6}$$

To infer $V(t)$ geometrical volume of air at a given time t, we consider measured input (outlet) flow during the recharge (discharge) phases, with the corresponding air temperature and pressure to rewrite the ideal gas law under changing number of molecules

$$V(t) = \frac{\left(n_0 + \int_{t_0}^{t} \Delta n(\tau) d\tau\right) R\, T(t)}{p(t)} \tag{7}$$

Eventually, we integrate this equation in time to infer the air volume inside the air reservoir at any given time, with known temperature and pressure during the processes with non-zero net airflow.

Details of pneumatic circuits used in the demonstrators. Based on the pneumatic circuit design in Fig. 1a, we include self-oscillating tube actuators[50] as a load in the thermopneumatic circuit to demonstrate the potential for motion and locomotion. In Fig. S18a, we include a single self-oscillating tube actuator in series with the outlet of the pressure-release valve. For demonstrating locomotion capabilities instead, we include two self-oscillating tube actuators in parallel with a pull-down resistor at the outlet of the pressure-release valve as shown in Fig. S18b.

Data availability

The data and code used in this study are available at https://doi.org/10.5281/zenodo.18244375. All data needed to evaluate the conclusions in the paper are present in the main manuscript paper and the Supplementary Materials.

References

1. Cho, K.-J. *2019 14th ACM/IEEE International Conference on Human-Robot Interaction (HRI)* (IEEE, 2019).
2. Stella, F. & Hughes, J. The science of soft robot design: a review of motivations, methods and enabling technologies. *Front. Robot. AI* **9**, 1059026 (2023).
3. Paternò, L. & Lorenzon, L. Soft robotics in wearable and implantable medical applications: translational challenges and future outlooks. *Front. Robot. AI* **10**, 1075634 (2023).
4. Hawkes, E. W., Blumenschein, L. H., Greer, J. D. & Okamura, A. M. A soft robot that navigates its environment through growth. *Sci. Robot.* **2**, eaan3028 (2017).
5. Mahon, S. T., Buchoux, A., Sayed, M. E., Teng, L. & Stokes, A. A. *2019 2nd IEEE International Conference on Soft Robotics (RoboSoft)* 782–787 (2019).
6. Wang, Z., Hirai, S. & Kawamura, S. Challenges and opportunities in robotic food handling: a review. *Front. Robot. AI* **8**, 789107 (2022).
7. Liu, Y., Hou, J., Li, C. & Wang, X. Intelligent soft robotic grippers for agricultural and food product handling: a brief review with a focus on design and control. *Adv. Intell. Syst.* **5**, 2300233 (2023).
8. Rajappan, A. et al. Logic-enabled textiles. *Proc. Natl. Acad. Sci. USA* **119**, e2202118119 (2022).
9. Patel, D. K. et al. Highly dynamic bistable soft actuator for reconfigurable multimodal soft robots. *Adv. Mater. Technol.* **8**, 2201259 (2022).
10. Lee, W.-K. et al. A buckling-sheet ring oscillator for electronics-free, multimodal locomotion. *Sci. Robot.* **7**, eabg5812 (2022).
11. Wang, T. et al. Mechanical intelligence simplifies control in terrestrial limbless locomotion. *Sci. Robot.* **8**, eadi2243 (2023).
12. Oliveri, G., van Laake, L. C., Carissimo, C., Miette, C. & Overvelde, J. T. B. Continuous learning of emergent behavior in robotic matter. *Proc. Natl. Acad. Sci. USA* **118**, e2017015118 (2021).
13. Tang, Y. et al. Leveraging elastic instabilities for amplified performance: spine-inspired high-speed and high-force soft robots. *Sci. Adv.* **6**, eaaz6912 (2020).
14. Shah, D. S. et al. A soft robot that adapts to environments through shape change. *Nat. Mach. Intell.* **3**, 51–59 (2020).
15. Baines, R. et al. Multi-environment robotic transitions through adaptive morphogenesis. *Nature* **610**, 283–289 (2022).
16. Zhao, Y. et al. Sunlight-powered self-excited oscillators for sustainable autonomous soft robotics. *Sci. Robot.* **8**, eadf4753 (2023).
17. Hu, W., Lum, G. Z., Mastrangeli, M. & Sitti, M. Small-scale soft-bodied robot with multimodal locomotion. *Nature* **554**, 81–85 (2018).
18. Kaynak, M., Dolev, A. & Sakar, M. S. 3d printed acoustically programmable soft microactuators,. *Soft Robot.* **10**, 246 (2023).
19. Sanchez, V. et al. Smart thermally actuating textiles. *Adv. Mater. Technol.* **5**, 2000383 (2020).
20. Drotman, D., Jadhav, S., Sharp, D., Chan, C. & Tolley, T. Electronics-free pneumatic circuits for controlling soft-legged robots. *Sci. Robot.* **6**, eaay2627 (2021).
21. Fusi, G., Del Giudice, D., Skarsetz, O., Di Stefano, S. & Walther, A. Autonomous soft robots empowered by chemical reaction networks. *Adv. Mater.* **35**, 2209870 (2022).
22. Lyu, L. X. et al. Bio-inspired untethered fully soft robots in liquid actuated by induced energy gradients. *Natl. Sci. Rev.* **6**, 970–981 (2019).
23. Aubin, C. A. et al. Towards enduring autonomous robots via embodied energy. *Nature* **602**, 393–402 (2022).
24. Louis, R. & Shea, K. Solar-powered thermo-pneumatic actuators for passively controlled adaptive shading. *Smart Mater. Struct.* **33**, 125034 (2024).
25. Sogabe, M., Uetrecht, F. C., Kanno, T., Miyazaki, T. & Kawashima, K. A quick response soft actuator by miniaturized liquid-to-gas phase change mechanism with environmental thermal source. *Sens. Actuators A: Phys.* **361**, 114587 (2023).
26. Boley, J. W. et al. Shape-shifting structured lattices via multimaterial 4d printing. *Proc. Natl. Acad. Sci. USA* **116**, 20856–20862 (2019).
27. Jeong, H. Y., Lee, E., Ha, S., Kim, N. & Jun, Y. C. Multistable thermal actuators via multimaterial 4d printing. *Adv. Mater. Technol.* **4**, 1800495 (2018).
28. Zhao, Y. et al. Twisting for soft intelligent autonomous robot in unstructured environments. *Proc. Natl. Acad. Sci. USA* **119**, e2200265119 (2022).
29. Chi, Y., Hong, Y., Zhao, Y., Li, Y. & Yin, J. Snapping for high-speed and high-efficient butterfly stroke-like soft swimmer. *Sci. Adv.* **8**, eadd3788 (2022).
30. Jumet, B., Bell, M. D., Sanchez, V. & Preston, D. J. A data-driven review of soft robotics. *Adv. Intell. Syst.* **4**, 2100163 (2021).
31. Lu, Q. et al. *Proceedings of the 36th Annual ACM Symposium on User Interface Software and Technology*, UIST '23 (ACM, 2023).
32. Shveda, R. A. et al. A wearable textile-based pneumatic energy harvesting system for assistive robotics. *Sci. Adv.* **8**, eabo2418 (2022).
33. Chun, H.-T. D., Taylor, N. K. & Stokes, A. A Energy-based abstraction for soft robotic system development. *Adv. Intell. Syst.* **5**, 2000264 (2021).
34. Mazzolai, B. & Laschi, C. A vision for future bioinspired and biohybrid robots. *Sci. Robot.* **5**, eaba6893 (2020).
35. Nakahara, K., Narumi, K., Niiyama, R. & Kawahara, Y. *2017 IEEE International Conference on Robotics and Automation (ICRA)* (IEEE, 2017).
36. Exley, T. et al. Agonist-antagonist pouch motors: bidirectional soft actuators enhanced by thermally responsive peltier elements (2024).
37. Uramune, R. et al. Hapouch: a miniaturized, soft, and wearable haptic display device using a liquid-to-gas phase change actuator. *IEEE Access* **10**, 16830–16842 (2022).
38. Garrad, M., Soter, G., Conn, A. T., Hauser, H. & Rossiter, J. *2019 2nd IEEE International Conference on Soft Robotics (RoboSoft)* (IEEE, 2019).
39. Nishikawa, Y. & Matsumoto, M. A design of fully soft robot actuated by gas-liquid phase change. *Adv. Robot.* **33**, 567–575 (2019).
40. Shahabi, E., Shabani, M., Meder, F. & Mazzolai, B. Solar spectrum light-driven silicone-based fluidic actuators. *Adv. Phys. Res.* (2024).
41. Hirai, S. et al. Micro elastic pouch motors: elastically deformable and miniaturized soft actuators using liquid-to-gas phase change. *IEEE Robot. Autom. Lett.* **6**, 5373–5380 (2021).
42. Kang, D. J., An, S., Yarin, A. L. & Anand, S. Programmable soft robotics based on nano-textured thermo-responsive actuators. *Nanoscale* **11**, 2065–2070 (2019).
43. Hao, B. et al. Focused ultrasound enables selective actuation and newton-level force output of untethered soft robots. *Nat. Commun.* **15**, 5197 (2024).
44. Kim, Y. I., Kim, S. W., An, S., Yarin, A. L. & Yoon, S. S. Untethered nanotextured thermopneumatic soft actuators operable with different stimuli: thermal blowing, infrared light, and electromagnetic field. *Int. J. Energy Res.* **2023**, 1–12 (2023).
45. Deglurkar, S., Xiao, C., Gockowski, L., Valentine, M. T. & Hawkes, E. W. A light- and heat-seeking vine-inspired robot with material-level responsiveness. *IEEE Robot. Autom. Lett.* **9**, 1–8 (2024).
46. Abolhosen, A. M. R. et al. Functional soft robotic composites based on organic photovoltaic and dielectric elastomer actuator. *Sci. Rep.* **14**, 9953 (2024).

47. Preston, D. J. et al. Digital logic for soft devices. *Proc. Natl. Acad. Sci. USA* **116**, 7750 (2019).
48. van Laake, L. C., Comoretto, A. & Overvelde, J. T. On the coexistence of pressure regulation and oscillation modes in soft hysteretic valves. *J. Fluids Struct.* **126**, 104090 (2024).
49. Galloni, E., Fontana, G. & Staccone, S. Design and experimental analysis of a mini ORC (organic rankine cycle) power plant based on R245fa working fluid. *Energy* **90**, 768–775 (2015).
50. Comoretto, A., Schomaker, H. A. H. & Overvelde, J. T. B. Physical synchronization of soft self-oscillating limbs for fast and autonomous locomotion. *Science* **388**, 610 (2025).
51. Liu, J., Li, P., Huang, Z., Liu, H. & Huang, T. Earthworm-inspired multimodal pneumatic continuous soft robot enhanced by winding transmission. *Cyborg Bionic Syst.* **6**, 0204 (2025).
52. Kandhari, A., Wang, Y., Chiel, H. J., Quinn, R. D. & Daltorio, K. A. An analysis of peristaltic locomotion for maximizing velocity or minimizing cost of transport of earthworm-like robots. *Soft Robot.* **8**, 485–505 (2021).
53. Sakes, A. et al. Shooting mechanisms in nature: a systematic review. *PLoS ONE* **11**, e0158277 (2016).
54. Kohlmeyer, J. & Volkmann-Kohlmeyer, B. Fungi on Juncus roemerianus. 6. glomerobolus gen. nov., the first ballistic member of agonomycetales. *Mycologia* **88**, 328–337 (1996).
55. Li, S., Zhang, Y. & Liu, J. Seed ejection mechanism in an oxalis species. *Sci. Rep.* **10**, 8855 (2020).
56. Deban, S. M., O'Reilly, J. C., Dicke, U. & van Leeuwen, J. L. Extremely high-power tongue projection in plethodontid salamanders. *J. Exp. Biol.* **210**, 655 (2007).
57. Karabulut, A. et al. The architecture and operating mechanism of a cnidarian stinging organelle. *Nat. Commun.* **13**, 3494 (2022).
58. An, B. et al. *Proceedings of the 2018 CHI Conference on Human Factors in Computing Systems*, CHI '18 (ACM, 2018).
59. Born, L. *Flectofold und Flectoline - Entwicklung adaptiver Fassadenbauteile aus Faserverbundkunststoff* (2023).
60. Luo, D. et al. Autonomous self-burying seed carriers for aerial seeding. *Nature* **614**, 463–470 (2023).
61. Yan, W. et al. Self-sustained, continuous jumping of a light-driven electronics-free insect-scale soft robot. *Adv. Mater.* (2025).
62. Gelebart, A. H. et al. Making waves in a photoactive polymer film. *Nature* **546**, 632–636 (2017).
63. Zheng, C. & Jia, S. Bioinspired photoresponsive soft robotic lens. *Sci. Robot.* **10**, eadw8905 (2025).
64. MVRDV. *Sombra* (accessed 08 December 2025) https://www.mvrdv.com/projects/1223/sombra (2025).
65. Cheng, T. et al. Weather-responsive adaptive shading through biobased and bioinspired hygromorphic 4D-printing. *Nat. Commun.* **15**, 10366 (2024).
66. Picella, S., van Riet, C. M. & Overvelde, J. T. B. Pneumatic coding blocks enable programmability of electronics-free fluidic soft robots. *Sci. Adv.* **10**, eadr2433 (2024).
67. Robin, A. C. Paper bag problem. *Bull. Inst. Math. Appl.* **40**, 104–107 (2004).
68. Wang, J. et al. Hybrid films with excellent oxygen and water vapor barrier properties as efficient anticorrosive coatings. *RSC Adv.* **8**, 21651–21657 (2018).
69. Shepherd, R. F. et al. Using explosions to power a soft robot. *Angew. Chem. Int. Ed.* **52**, 2892–2896 (2013).
70. Aubin, C. A. et al. Powerful, soft combustion actuators for insect-scale robots. *Science* **381**, 1212–1217 (2023).
71. Bell, M. A., Gorissen, B., Bertoldi, K., Weaver, J. C. & Wood, J. A modular and self-contained fluidic engine for soft actuators. *Adv. Intell. Syst.* **4**, 2100094 (2021).
72. Gollob, S. D. et al. *2025 IEEE 8th International Conference on Soft Robotics (RoboSoft)* 1–8 (IEEE, 2025).
73. Fonseca, D. & Neto, P. Electrically-driven phase transition actuators to power soft robot designs. *Nat. Commun.* **1**, 3920 (2025).
74. Gockowski, L. F. et al. Improving the efficiency of soft phase-change actuators using thermodynamic analysis. *Soft Robot.* **12**, 687–697, (2025).
75. Adami, M. & Seibel, A. On-board pneumatic pressure generation methods for soft robotics applications. *Actuators* **8**, 2 (2018).
76. Liga, A. et al. Study on heat transfer coefficients during cooling of PET bottles for food beverages. *Heat. Mass Transf.* **52**, 1479–1488 (2015).
77. Saggin, B. et al. Non-contact measurement of the temperature profile of pet preforms. *Measurement* **133**, 412–420 (2019).
78. Meng, D. et al. Polyethylene terephthalate-based colored emitters for efficient daytime radiative cooling. *Results Phys.* **46**, 106254 (2023).
79. Wyngaard, J. C. Book review: atmospheric turbulence. Models and methods for engineering applications by Hans A. Panofsky and John A. Dutton. *AIAA J.* **23**, 2008–2009 (1985).
80. Cengel, Y. A. & Boles, M. A. *Thermodynamics: An Engineering Approach*, 8th edn. (McGraw-Hill Professional, 2014).
81. Hellmann, G. Über die Bewegung der Luft in den untersten Schichten der Atmosphäre: erste Mitteilung. In *Sitzungsberichte der Königlich Preußischen Akademie der Wissenschaften: Jahrgang 1914, Erster Halbband Januar bis Juni* (1914).
82. Wan, S. et al. Estimates of wind speed profiles from surface observations: machine learning versus Monin–Obukhov approach. *Bound.-Layer Meteorol.* **191** https://doi.org/10.1007/s10546-025-00903-2 (2025).
83. Tennekes, H. The logarithmic wind profile. *J. Atmos. Sci.* **30**, 234–238 (1973).
84. Kaimal, J. C. & Finnigan, J. J. *An Introduction to Boundary Layer Meteorology* https://doi.org/10.1007/978-94-009-3027-8 (Springer, 1988).
85. Rahmani, A., Chouaf, F., Bouzid, L. & Bedoui, S. Experimental evaluation of the wind convection heat transfer on the glass cover of the single-slope solar still. *Heat. Transf.* **53**, 1292–1311 https://doi.org/10.1002/htj.22997 (2024).
86. Kumar, S., Sharma, V. B., Kandpal, T. C. & Mullick, S. C. Wind induced heat losses from outer cover of solar collectors. *Renew. Energy* **10**, 613–616 https://doi.org/10.1016/S0960-1481(96)00031-6 (1997).
87. Sharples, S. & Charlesworth, P. S. Full-scale measurements of wind-induced convective heat transfer from a roof-mounted flat plate solar collector. *Sol. Energy* **62**, 69–77 https://doi.org/10.1016/S0038-092X(97)00119-9 (1998).
88. Kumar, S. & Mullick, S. C. Wind heat transfer coefficient in solar collectors in outdoor conditions. *Sol. Energy* **84**, 956–963 https://doi.org/10.1016/j.solener.2010.03.003 (2010).

Acknowledgements

We thank all members of our Soft Robotic Matter Group for the invaluable discussions. We are grateful to N. Commandeur for technical support.

Author contributions

Conceptualization: S.P. and J.T.B.O. Methodology: all authors. Investigation: S.P., O.V., and A.C. Data analysis: S.P. Visualization: S.P. Supervision: J.T.B.O. Writing: S.P. and J.T.B.O. Review and editing: all authors.

Funding

This project has received funding from the European Union's 2020 ERC-STG under grant agreement no. 948132. This work is part of the Dutch Research Council (NWO) and was performed at the research institute AMOLF.

Competing interests
The authors declare no competing interests.

Additional information
Supplementary information The online version contains supplementary material available at https://doi.org/10.1038/s41467-026-77422-2.

Correspondence and requests for materials should be addressed to Johannes T. B. Overvelde.

Peer review information *Nature Communications* thanks the anonymous reviewers for their contribution to the peer review of this work. A peer review file is available.

Reprints and permissions information is available at http://www.nature.com/reprints

Publisher's note Springer Nature remains neutral with regard to jurisdictional claims in published maps and institutional affiliations.

Open Access This article is licensed under a Creative Commons Attribution-NonCommercial-NoDerivatives 4.0 International License, which permits any non-commercial use, sharing, distribution and reproduction in any medium or format, as long as you give appropriate credit to the original author(s) and the source, provide a link to the Creative Commons licence, and indicate if you modified the licensed material. You do not have permission under this licence to share adapted material derived from this article or parts of it. The images or other third party material in this article are included in the article's Creative Commons licence, unless indicated otherwise in a credit line to the material. If material is not included in the article's Creative Commons licence and your intended use is not permitted by statutory regulation or exceeds the permitted use, you will need to obtain permission directly from the copyright holder. To view a copy of this licence, visit http://creativecommons.org/licenses/by-nc-nd/4.0/.

© The Author(s) 2026

This Article in Press is shared early to give you faster access to new research. It is citable and carries a permanent DOI. The final edited version will replace it automatically.